# e-ISSN: 2812-9709

# TOTAL ENTROPY AND EXERGY EFFICIENCY OF GRAPHENE OXIDE/NANODIAMOND HYBRID NANOFLUIDS IN A MINI HEAT SINK: EXPERIMENTAL AND PARTICLE SWARM OPTIMIZATION PREDICTIONS

Original scientific paper

UDC:62-713.3

https://doi.org/10.46793/adeletters.2025.4.2.2

# L. Syam Sundar<sup>1\*</sup>

<sup>1</sup>Department of Mechanical Engineering, College of Engineering, Prince Mohammad Bin Fahd University, Al Khobar, 31952, Saudi Arabia

#### Abstract:

Through the Particle Swarm Optimization (PSO), the thermal entropy, frictional entropy, entropy generation ratio, entropy generation number, and exergy efficiency of reduced graphene oxide/nanodiamond (rGO/ND) hybrid nanofluids flow in a mini-heat sink were predicted after being measured experimentally. A 60:40% (weight percentage) water and ethylene glycol mixture was used as the base fluid in this study. The experiments were conducted under different volume loadings ( $0 \le \phi \le$ 2%), and different Reynolds numbers  $(1393.75 \le Re \le 5861.44)$ . Eventually, the thermophysical properties were also estimated. The thermal entropy generation of 2.0% vol. was decreased by 34.87%, and frictional entropy generation and exergy efficiency were raised by 21.30% and 18.10% at a Reynolds number of 4181.24 over the base fluid. The PSO artificial neural network method was used in this study. The PSO predictions data have shown a good acceptance with the experimental values with root-mean-square errors of 0.058262, 4.9088e-05, 0.0034824, 0.015519, and 0.050993, with correlation coefficients of 0.99811, 0.99218, 0.99849, 0.99812, and 0.99571, for thermal entropy, frictional entropy, entropy generation ratio, entropy generation number, and exergy efficiency, respectively. Based on the polynomial regression analysis, new thermal entropy generation, frictional entropy generation, entropy generation number, and exergy efficiency correlations were proposed.

#### **ARTICLE HISTORY**

Received: 29 April 2025 Revised: 7 June 2025 Accepted: 17 June 2025 Published: 30 June 2025

#### **KEYWORDS**

Thermal entropy,
Frictional entropy,
Particle swarm optimization,
Enhancement,
Nanofluids

#### 1. INTRODUCTION

For constant functioning, electronic equipment such as laptops and personal computers must be operated within a specific temperature range. Allowing the maximum temperature to be exceeded for these devices was quite risky. To maintain a steady operating temperature, the cooling system must remove heat from the equipment. Air conditioning systems previously cooled the small heat sink. Using air as a cooling medium, Egan et al. [1] examined a small heat sink of 534 mm<sup>2</sup> and having a profile height of 5 mm. They discovered a

20% increase in thermal performance. Mohamed and El-Baky [2] examined two small channel heat sinks, one with a rectangular shape measuring 5×18 mm² and the other with a triangular shape measuring 5×9 mm². They discovered that there was more heat transfer to the air side when the mass flow rate and channel bottom temperature increased, and they also suggested a correlation. It was challenging to achieve enhanced cooling performance due to the limitations of this conventional air-cooling approach. As a result, liquid cooling replaces air cooling. Peng and Peterson [3]

investigated the flow patterns and heat transfer in a micro-channel with water. Qu and Mudawar [4] investigated heat transfer and the drop-in water pressure as it went through a micro-channel heat sink. Three different types of micro heat sinks, including rectangular, trapezoidal, and hexagonal, were examined by Makam and Totla [5]. They conducted studies in laminar flow (200 < Re < 1000) and found increased heat transfer rates. In their computational analysis of heat transfer for both rectangular and circular heat sinks operating with water, Ghasemi et al. [6] found that the rectangular cross-section heat sink had higher heat transfer rates than the circular channel heat sink.

High-thermal-conductivity fluids can be used to replace the single-phase fluid in the tiny heat sink to further increase its heat transfer rates. By mixing nanoscale particles into the base fluid, Choi and Eastman [7] created the high thermal conductivity "nanofluids". fluids known as Subsequently, researchers have acquired increased thermal conductivity compared with the base fluid. Watermixed Al<sub>2</sub>O<sub>3</sub>, MgO, and TiO<sub>2</sub> nanofluids were prepared by Mukherjee et al. [8] and used in a mini heat sink. They observed that the Al<sub>2</sub>O<sub>3</sub>, MgO, and TiO<sub>2</sub> nanofluids performed better increasing heat transfer by 24.95%, thermal resistance by 15.01%, 19.96%, and total entropy generation by respectively.

Thrush et al. [9] used zirconia (ZrO<sub>2</sub>)/polyalphaolefin (PAO) base oil; Barbés et al. [10] used CuO/water and ethylene glycol; and Agarwal et al. [11] used Al<sub>2</sub>O<sub>3</sub>/water and ethylene glycol. As a result, small heat sinks are using nanofluids to increase heat transfer efficiency. The experimental investigation of Cu/water nanofluid by Chein and Huang [12] showed enhanced thermal performance in micro-channel heat sinks. Lee and Mudawar [13] examined water-mixed Al<sub>2</sub>O<sub>3</sub> coolant using a micro-channel heat sink and found improved heat transfer properties. In a triangular micro heat sink, Sheik et al. [14] employed SiO<sub>2</sub>/water nanofluids and discovered increases in the thermal performance factor of 2.17 and 1.75 for SiO<sub>2</sub> nanofluid and water, respectively. With the aid of CuO nanofluids and water-diluted Al<sub>2</sub>O<sub>3</sub>, Seyf and Mohammadian [15] quantitatively measured a 13.7% and 4.9% increase in thermal performance in the micro-channel heat sink, respectively. In a divergent-convergent mini-channel heat sink, Sidik discovered quantitatively [16] a thermal performance gain of 6.44% and 8.33% for 2.5 vol% of water-dispersed Al<sub>2</sub>O<sub>3</sub> and CuO nanofluids. Using experimental data of CuO nanofluids diluted with water passing through a heat sink, Selvakumar and Suresh [17] estimated a 29.63% increase in heat transfer and a 15.11% increase in pumping power in comparison to water. A 10% reduction in thermal resistance was discovered by Fazeli et al. [18] when water-dispersed SiO2 was used in a small heat sink.

The experiment by Nguyen et al. [19] showed that when the electronic component was cooled using an Al<sub>2</sub>O<sub>3</sub>/water nanofluid, its heat transfer increased to 40% at 6.8% vol. Ho et al. [20] observed a figure-ofmerit of 1.098 at a Reynolds number of 1381 with heat flux of 4.78 W cm<sup>-2</sup> at 2% (mass) in a small heat sink using water diluted nanophase transition materials. When Ho and Chen [21] investigated using an Al<sub>2</sub>O<sub>3</sub>/water nanofluid as a coolant in place of pure water in a copper mini-channel heat sink, they observed noticeably improved average heat transfer coefficients. Patel et al. [22] observed a 3.05% increase in heat transfer and a 47.8% rise in the Nusselt number at 5 vol% of EG20 nanofluid, based on a numerical study. In comparison to other nanofluids, Saadoon et al. [23] found that the Nusselt number of Ag/water nanofluids reached to 54% at 0.075% vol. CuO, Dimond, Al2O3, Fe3O4, TiO2, and Ag nanofluids based on water with volume of concentration of 0.075%.

Hybrid nanofluids can further improve the mini heat sink's heat transfer rates. It was first important to determine whether the hybrid nanofluids have a higher thermal conductivity before using them in a mini heat sink. Sundar et al. [24-26] discovered improved thermal conductivity compared to mono nanofluids using MWCNT-Fe<sub>3</sub>O<sub>4</sub>/water nanofluids, ND-Co<sub>3</sub>O<sub>4</sub>/water hybrid nanofluids, and nanodiamond-Fe<sub>3</sub>O<sub>4</sub> hybrid nanofluids. Al<sub>2</sub>O<sub>3</sub>-ZnO/water hybrid nanofluids were created by Wole-Osho et al. [27], while Dalkılıç et al. [28] created hybrid nanofluids of CNT and SiO<sub>2</sub>. Al<sub>2</sub>O<sub>3</sub>-SiO<sub>2</sub>/water hybrid nanofluids were created by Yıldız et al. [29], while Al<sub>2</sub>O<sub>3</sub>-SiO<sub>2</sub>/water hybrid nanofluids were created by Moldoveanu et al. [30], who discovered that they had higher thermal conductivity than mono nanofluids. Therefore, it was known that the thermal conductivity of hybrid nanofluids was higher than that of mono nanofluids.

Below is a discussion of the works that pertain to the usage of hybrid nanofluids in small heat sinks. In a review study, Sriharan et al. [31] discussed the fabrication of hybrid nanofluids and the investigation of heat transport in small heat sinks. CuO,  $TiO_2$ , and  $Fe_2O_3$  based on water were used in mini-channel heat sink heat transfer experiments by Baig et al. [32]. Water-based CuO- $TiO_2$  and CuO- $Fe_2O_3$  hybrid nanofluids were found to enhance heat transfer by

29.24% and 24.55%, respectively, over water data at a Reynolds number of 750 for CuO, CuO 0.75%+Fe<sub>2</sub>O<sub>3</sub> 0.25%. In a tiny heat sink, Sriharan et al. [33] employed water-based Al<sub>2</sub>O<sub>3</sub>-SiO<sub>2</sub>, Al<sub>2</sub>O<sub>3</sub>/CuO, and CuO/SiO<sub>2</sub> hybrid nanofluids, and they found that the Al<sub>2</sub>O<sub>3</sub>/CuO-water nanofluids improved the Nusselt number, heat transfer coefficient, and effectiveness by 54.5%, 42%, and 28.4%, respectively. Kumar and Sarkar [34] have reported that the heat transfer was improved by 8.5% and 12.8% using computational and experimental methods for Al<sub>2</sub>O<sub>3</sub>-TiO<sub>2</sub>/water in a mini heat sink. Kumar and Sarkar [35] investigated heat transfer numerically under laminar flow in a mini-channel heat sink using water diluted Al<sub>2</sub>O<sub>3</sub> and Al<sub>2</sub>O<sub>3</sub>-MWCNT nanofluids. They discovered a 15.6% improvement in maximum heat transfer coefficient at 0.01 vol.% without an increase in pressure drop. These studies show that hybrid nanofluids have higher heat transfer rates than micro heat sinks.

It was acknowledged that the heat transfer data for the mini heat sink associated with reduced graphene oxide (rGO)/nanodiamond (ND) nanofluids was not provided. Field effect transistors, energy storage, composite materials, gas sensing, and high conductivity are among applications for the rGO. In a similar vein, nanodiamonds (NDs) are good functional materials that find application in the semiconductor and development industries for tool surface modification, polishing, and grinding. It shows good hardness and thermal conductivity qualities when combined with rGO/ND hybrid nanoparticles.

Raising the freezing point of water (W) was possible by a few degrees Celsius by adding modest amounts of ethylene glycol (EG). In order to preserve the excellent heating (or cooling) properties of water and to increase the operational temperature range for energy applications, water mixture EG was a type of heat transfer fluid that was frequently utilized in numerous energy systems. The W/EG combination may be used for heating and ventilation purposes as well as automobile engine coolant in most colder nations, including Canada, Alaska, Russia, and others. The most often utilized heat transfer fluid was a 60:40% W/EG. Therefore, 60:40% (wt) water and ethylene glycol-based rGO/ND hybrid nanofluids were created for the current investigation, and their flow via a tiny heat sink was monitored for thermal entropy, frictional entropy, and exergy efficiency phenomena. The 70:30% (weight) hybrid nanoparticles of rGO and ND were considered. Experimental methods were used to determine thermophysical characteristics. Experimental estimates are also made for the entropy generation umber, entropy generation ratio, and exergy efficiency under turbulent flow with volume loadings ranging from 0% to 2%. The PSO artificial neural network algorithm was used to forecast the obtained data. The experimental findings led to the proposal of new correlations.

#### 2. MATERIAL AND METHODS

The chemicals, lincluding graphite powder, sodium nitrate (NaNO<sub>3</sub>), hydrogen peroxide ( $H_2O_2$ ), ethylene glycol ( $C_2H_6O_2$ ), potassium permanganate (KMnO<sub>4</sub>), hydrochloric acid (HCl), sulfuric acid ( $H_2SO_4$ ), and nitric acid (HNO<sub>3</sub>) were acquired from Sigma-Aldrich Chemicals, USA manufacturer. The nanodiamond (ND) soot was obtained from International Technology Center, USA manufacturer. The distilled water was also used.

# 2.1. Preparation of Reduced Graphene Oxide Nanosheets

The reduced graphene oxide nanosheets were prepared based on the procedure given by Zaaba et al. [36]. The procedure involved dissolving 10 g of graphite powder in 200 mL of H<sub>2</sub>SO<sub>4</sub> and 0.025 M of NaNO<sub>3</sub>. The liquid was then cooled in an ice water bath for 30 minutes. Following the addition of 0.039 M KMnO<sub>4</sub>, the entire complex was vigorously stirred using an agitator for 20 minutes at a temperature of 0°C. The solution becomes green due to the presence of the oxidizing agent Permanganyl ion (MnO<sup>3+</sup>). Room temperature was attained by extracting them from the ice water bath. The solution underwent an additional treatment using a 30 wt.% concentration of H<sub>2</sub>O<sub>2</sub> for approximately 30 minutes to eliminate any remaining contaminants, after thorough cleaning with significant amounts of distilled water. The reduced graphene oxide (rGO) nanosheets were ultimately obtained by extracting them from water using the centrifugal technique. The reduced graphene oxide (rGO) was exposed to a temperature of 60°C for approximately 12 hours.

When GO was synthesized using Hummers' process, metal ions such as Mn<sup>2+</sup> and Fe<sup>3+</sup>, along with other impurities, may still be present. By creating metal chlorides, strong acids efficiently eliminate impurities, cleaning the surface and releasing reactive sites for carboxylation. Following reduction, graphene oxide (GO) typically retains residual oxygen functionalities, including carbonyl (C=O), hydroxyl (–OH), and epoxide (–O–) groups. In order to increase the reactivity of these oxygen-containing groups and facilitate their subsequent hydrolysis or

oxidative reactions to become carboxylic acid groups, they can be protonated using a 1:3 molar ratio of  $H_2SO_4$  and  $HNO_3$  and stirred with a magnetic stirrer for 72 hours. To obtain a large number of rGO nanosheets, the same process was performed multiple times.

#### 2.2. Purification of Nanodiamond Soot

The nanodiamond-soot was purified with the assistance of Sundar et al. [37]. The process involves dispersing 10 g of ND-soot in 200 MI of distilled water and then agitating it with a magnetic stirrer for 30 minutes. The detonation procedure, which uses a weight ratio of 50:50% for TNT (trinitrotoluene) and RDX (cyclotrimethylenetrinitramine), is typically used to create ND nanoparticles. Amorphous carbon and other contaminants surround the ND particles in the resulting ND. To extract pure diamond nanoparticles, a strong acid treatment necessary. To do this, the resulting ND-soot was treated with a mixture of sulfuric and nitric acids in a 1:3 molar ratio, and the mixture was stirred for 72 hours. While the nanoparticles were dispersed in the base fluid, this process facilitated the removal of contaminants from the ND-soot, the production of carboxyl groups on the surface of the ND particles, and the attachment of the nanoparticles to the rGO nanosheet. The ND-soot was then repeatedly rinsed with distilled water.

# 2.3. Preparation of Hybrid Nanofluids and Properties

Before preparing the hybrid nanofluids, the physical properties of hybrid nanoparticles were estimated from mixture formulas. Nanoparticles of 70:30% (weight percentage) were considered in this study.

(a) Thermal conductivity,

$$k_{(rGO/ND)_p} = \frac{k_{rGO} \times W_{rGO} + k_{ND} \times W_{ND}}{W_{rGO} + W_{ND}}$$
 (1)

(b) Density of particles,

$$\rho_{(rGO/ND)_p} = \frac{\rho_{rGO} \times W_{rGO} + \rho_{ND} \times W_{ND}}{W_{rGO} + W_{ND}}$$
(2)

(c) Specific heat,

$$C_{p_{(rGO/ND)_p}} = \frac{C_{p,rGO} \times W_{ND} + C_{p,ND} \times W_{ND}}{W_{rGO} + W_{ND}}$$
(3)

where are: k,  $\rho$ , and  $\mathcal{C}_p$  stands for thermal conductivity, density, and specific heat, respectively. The rGO and ND were reduced graphene oxide, and nanodiamond, W stands for weight. The physical properties of base fluid and nanoparticles are given in Table 1.

Table 1. Properties of substances and base fluid at 20°C

	Substances					
Property	Base fluid NI		rGO	rGO/ND		
	(60:40% W/EG)			(70:30%)		
ho (kg/m <sup>3</sup> )	1059.65	3100	1910	2267		
k (W/mK)	0.404	2200	4000	3460		
μ (mPa·s)	2.94					
$C_p$ (J/kgK)	3402	610	710	680		

The hybrid nanofluids were prepared at volume loadings of 0.5%, 1.0%, 1.5%, and 2.0% by direct blending of hybrid particles in a 60:40% W/EG fluid. Out of 10 g of hybrid particles, there are 7 and 3 g of rGO and ND particles. Similarly, the base fluid was 60:40% (weight) W/EG and through Eq. (2), the density of rGO/ND was calculated and used in Eq. (4) to determine the required quantity of nanoparticles for the known volume loadings.

Volume concentration:

$$\phi = \frac{\left[\frac{W_{rGO/ND}}{\rho_{rGO/ND}}\right]}{\left[\frac{W_{rGO/ND}}{\rho_{rGO/ND}}\right] + \left[\frac{W_{basefluid}}{\rho_{basefluid}}\right]} \times 100 \tag{4}$$

A total of 10 kg of base fluid was used, in which 6 kg of water and 4 kg of ethylene glycol were used to match 60:40% (weight) of W/EG mixture, in which 86.01, 172.88, 260.64, and 349.29 g of rGO/ND nanoparticles were used to match 0.5%, 1.0%, 1.5%, and 2.0%, volume loadings, respectively.

For the preparation of 0.5% vol., 10 kg of base fluid was placed in a 30 L drum and then added 86.01 g of hybrid nanoparticles and mixed vigorously with stirrer for 4 hrs. Similarly, the other nanofluids of 1.0%, 1.5%, and 2.0% were prepared by dispersing 172.88, 260.64, and 349.29 g of rGO/ND in 10 kg of base fluid and then stirred for 4 hrs with mechanical stirrer.

The produced nanofluids can be considered totally stable if the zeta potential value is more than -30 or +30 mV. Each nanofluid sample's zeta potential was evaluated using a Zetasizer instrument, and the results showed that the zeta potential values for 0.5%, 1.0%, 1.5%, and 2.0% of the volume of nanofluid were, respectively, -45 mV, -41 mV, -38 mV, and -36 mV. The zeta potential values are seen to be above the usual value of -30 mV, indicating the high stability of the generated hybrid nanofluids. The instruments were used to experimentally measure the fluid's properties, including density, viscosity, specific heat, and thermal conductivity.

The thermophysical properties required for the analysis of heat transfer were not available in the open literature. Hence, those were estimated experimentally. Instruments such as the KD-2 Pro (Decagon Devices in the USA, featuring a KS-1 sensor with a length of 60 mm and a diameter of 1.27 mm), the A&D viscometer (SV-10, Japan), a digital weighing machine, and a differential scanning calorimeter (Mettler-Toledo, USA) were used to evaluate the properties. The parameters were computed using Eqs. (5)-(8).

The obtained thermal conductivity  $(k_{nf})$  of rGO/ND nanofluids was raised by 5.69%, 8.66%, 10.15%, and 13.12% at 0.5%, 1.0%, 1.5%, and 2.0% vol. and at 20°C, against base liquid, the  $k_{nf}$  was further raised to 12.09%, 16.74%, 22.33%, and 25.35%, respectively, at 60°C (Fig. 1a). The obtained viscosity  $(\mu_{nf})$  of rGO/ND nanofluids was raised by 56.80%, 80.61%, 88.78%, and 96.60% at 20°C and at 0.5%, 1.0%, 1.5%, and 2.0% vol. against base liquid, and it was further raised to 16.95%, 33.90%, 45.76%, 53.39% at 60°C, over the base fluid (Fig. 1b). The density  $(\rho_{nf})$  of rGO/ND nanofluid variation of was noticed, under 2 vol%, it was 1083.82, and 1064.15 kg/m<sup>3</sup> at 20°C and 60°C, under the same temperatures, the base fluid density was 1059.6, and 1039.6 kg/m³ (Fig. 1c). The lower specific heat  $(C_{p,nf})$  of rGO/ND nanofluids of 3412.24 from 3454.06 J/kgK were seen for 2% vol, and at 20°C. Likewise, a lower  $C_{p,nf}$  of 3543.56 from 3602 J/kg K were seen for 2% vol, and at 60°C, respectively (Fig. 1d).

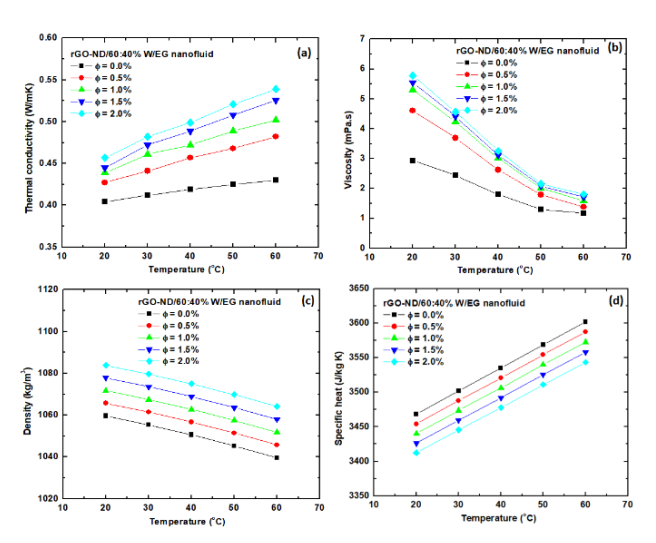


**Fig. 1.** Properties with respect to volume loadings, and temperatures, (a) thermal conductivity, (b) viscosity, (c) density, and (d) specific heat

The Prandtl number (*Pr*) was higher with increase of volume loadings, and was lesser with an increase of temperature. The *Pr* was 43.16 at 2% vol. of nanofluid, whereas, for base fluid, the *Pr* was 25.24, at 20°C, whereas, the *Pr* for 2.0% vol. of

nanofluid was 11.90, but for base fluid was 9.88 at 60°C, respectively.

$$k_{nf} = 0.36684 + 0.001514 T + 0.03924 \phi$$
 (5)

$$\mu_{nf} = 5.6724 - 0.08608 T + 0.746 \phi \tag{6}$$

$$\rho_{nf} = 1069.987 - 0.496543 T + 12.1722 \phi (7)$$

$$C_{p,nf} = 3402.54 + 3.3165T - 28.552 \,\phi$$
 (8)  $20^{\circ}C \le T \le 60^{\circ}C$ , and  $0 \le \phi \le 2.0\%$ .

# 2.4 Heat Sink Setup

Figure 2(a) depicts the schematic representation of an experimental arrangement. The data collecting systems, fixed water temperature bath, and heat sink were utilized. The primary constituent was a heat sink, which was a square aluminum block utilized for constructing the heat sink. It has dimensions of 50×50×10 mm (length × width × height). Within the block, four circular channels with a diameter of 4 mm were employed. Four 1 mm diameter holes, each with a depth of 20 mm, were drilled adjacent to the side wall of the heat sink's bottom surface for the purpose of mounting a thermocouple. All the thermocouples used in this experiment were calibrated and their accuracy was determined to be as low as ± 0.1 K. Four K-type thermocouples were inserted into the holes of the heat sink to gauge the temperature of the base plate. In addition, two K-type thermocouples are placed at the entrance and exit of the heat sink enclosure to monitor the temperature of the fluid as it enters and exits. A constant heat flux was being applied to the bottom of the block.

Figure 2(b) has a diagram of the heater block and heat sink. In order to create heat, two heaters with a diameter of 10 mm were utilized and positioned within the heater block. The polyurethane foam located at the base of the heater block was considered to be an insulating material that limits the transfer of heat from the heater block to the surrounding environment. To enhance efficiency of heat transmission, a high thermal conductive grease was applied to the gap between the heat sink and heater block. The pump facilitates the movement of the base fluid/hybrid nanofluid into the heat sink, and subsequently, the rate of flow was quantified. The temperature of the heat sink inlet was controlled by the F10-Hc Julabo uniform temperature bath, which was positioned above the pump. In order to maintain a constant temperature at the outlet, a cooler was employed to regulate the fluid temperature. The hybrid nanofluids cool due to the transfer of heat from the cold water in the reservoir to them.

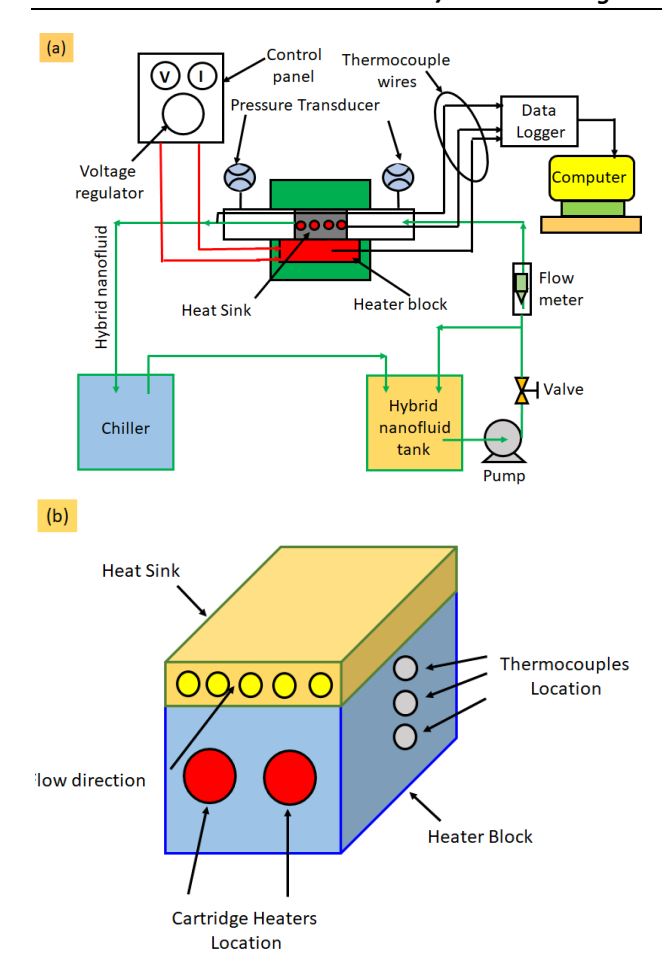


**Fig. 2.** (a) Line diagram of an experimental setup, and (b) test section details

By connecting the thermocouples to the logging device and then to the laptop, it is possible to monitor and record all temperatures concurrently. The Endress Hauser differential pressure transducer, which has been calibrated by the manufacturer, was used to monitor the decrease in pressure of the fluid in the heat sink. It has an accuracy of  $\pm\,2\%$  and can detect pressure within the range of 0 to 250 kPa. Both sides of the heat sink had connectors for the pressure transducers.

#### 3. PARTICLE SWARM OPTIMIZATION

Particle Swarm Optimization (PSO) is a powerful optimization algorithm that can be used to optimize the hyperparameters of an Artificial Neural Network (ANN) for regression tasks. The combination of PSO and ANN, known as a PSO-optimized ANN, can effectively model complex nonlinear relationships between input features and target variables. The line diagram of PSO is shown in Fig. 3.

In this approach, the ANN architecture (e.g., number of layers, neurons per layer) and hyperparameters (e.g., learning rate, momentum, regularization) are optimized using the PSO

algorithm. PSO was a population-based optimization technique that mimics the social behavior of bird flocks or fish schools. Each potential solution in the PSO algorithm was represented as a particle, and the particles moved through the search space, adjusting their position and velocity based on their own experience (local best) and the experience of the entire swam (global best).

The PSO algorithm starts by randomly initializing a population of particles, where each particle represents a potential set of ANN hyperparameters. The fitness of each particle was evaluated by training the ANN with the corresponding hyperparameters and measuring the performance on a validation dataset. The performance metric, such as mean squared error (MSE) was used as the fitness function in the proposed approach. Based on the particle's current position, its own best position (local best) i.e.  $p_i$ , and the global best position  $p_g$  of the swarm, the velocity  $(v_i)$  and position  $(x_i)$  of each particle are updated using the following Egs. (9)-(10):

$$v_{i}(t+1) = w \times v_{i}(t) + c_{1} \times r_{1} \times (p_{i} - x_{i}(t)) + c_{2} \times r_{2} \times (p_{g} - x_{i}(t))$$

$$x_{i}(t+1) = x_{i}(t) + y_{i}(t+1)$$
(10)

where are:  $c_1$ , and  $c_2$  are the cognitive and social learning rates, respectively; w was the inertia weight, which controls the influence of the particle's previous velocity. The r, and  $r_2$  are random numbers between 0 and 1.

After updating the particles' positions and velocities, the global best position  $p_g$  was updated if any particle has found a better solution. The optimization process continues until a specified termination condition is met, such as a maximum number of iterations or a target fitness value. The fitness function was expressed as follows,

where *net* represents the ANN network with updated hyperparameters.

Once the PSO optimization was complete, the ANN was trained using the best set of hyperparameters found by the algorithm. The data used for PSO analysis is shown in Table 2.

Table 2. The data used for the PSO analysis

Input		Output				
	Vol.	$\Psi_{gen,th}$				
Re	(%)	(W/K)	$\Psi_{gen,f}$	EGR	Ns	η (%)
1953.8	0	5.8513	0.000052		1.558	9.3
2605.0	0	4.7877	0.000115		1.275	9.31
3256.3	0	4.1038	0.000213		1.093	9.35
3907.6	0	3.6903	0.000353		0.983	9.36
4558.8	0	3.3009	0.000541		0.879	9.38
5210.1	0	3.1270	0.000783		0.832	9.43
5861.4	0	3.0156	0.001085		0.803	9.56
1726.1	0.5	5.0574	0.000054	0.864	1.347	9.46
2301.5	0.5	4.0839	0.000120	0.853	1.087	9.48
2876.9	0.5	3.4684	0.000222	0.845	0.923	9.51
3452.3	0.5	3.0941	0.000370	0.838	0.824	9.52
4027.6	0.5	2.7463	0.000565	0.832	0.731	9.54
4603	0.5	2.5837	0.000826	0.826	0.688	9.6
5178.4	0.5	2.4751	0.001153	0.820	0.659	9.69
1505.7	1	4.7273	0.000057	0.807	1.259	9.63
2007.7	1	3.8800	0.000127	0.810	1.033	9.66
2509.6	1	3.3033	0.000232	0.805	0.879	9.69
3011.5	1	2.9565	0.000387	0.801	0.787	9.71
3513.4	1	2.6051	0.000593	0.789	0.693	9.72
4015.4	1	2.4383	0.000869	0.779	0.649	9.78
4517.3	1	2.3268	0.001214	0.771	0.612	9.85
1441.0	1.5	4.4506	0.000059	0.760	1.185	9.75
1921.4	1.5	3.5966	0.000132	0.751	0.958	9.77
2401.7	1.5	3.0290	0.000246	0.738	0.806	9.81
2882.0	1.5	2.6945	0.000412	0.730	0.717	9.82
3362.4	1.5	2.3984	0.000632	0.726	0.638	9.83
3842.7	1.5	2.2340	0.000911	0.714	0.595	9.91
4323.1	1.5	2.1493	0.001274	0.712	0.572	10.01
1393.7	2	4.2541	0.000061	0.727	1.133	10.72
1858.3	2	3.3722	0.000137	0.704	0.898	10.72
2322.9	2	2.8103	0.000256	0.684	0.748	10.74
2787.5	2	2.5106	0.000422	0.680	0.668	10.84
3252.0	2	2.2252	0.000648	0.674	0.592	10.92
3716.6	2	2.0647	0.000935	0.660	0.550	11.07
4181.2	2	1.9640	0.001308	0.651	0.523	11.29

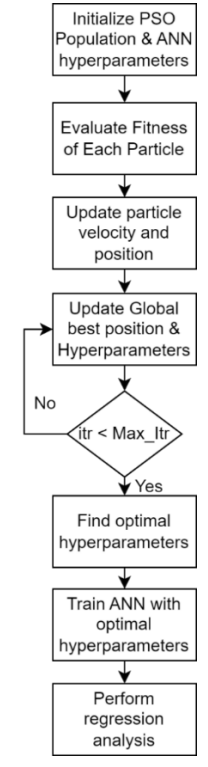


Fig. 3. Flow chart of particle swarm optimization

#### 4. RESULTS AND DISCUSSION

The hybrid nanofluids, consisting of a mixture of reduced graphene oxide (rGO) and nanodiamond (ND) at a ratio of 60:40%, were used in the apparatus at a temperature of 20°C. The nanofluids were exposed to a uniform heat flux of 64000 W/m<sup>2</sup>. The upper surface and lateral surfaces were sealed with insulating material. Initially, a base fluid consisting of 60% water and 40% ethylene glycol (W/EG) was utilized. Subsequently, nanofluids were added sequentially. The trials were conducted within the mass flow (m) rate range of 1.2 to 3.6 L/min. The Reynolds number (Re = 4m'/πdμ) was determined by considering the mass flow rate and viscosity of the fluid. The estimated value corresponds to the base fluid. The value was 1953.81. The Reynolds number ranges for different volumes are as follows: for a volume of 0.5%, the Reynolds number was between 1726.1 and 5178.4; for a volume of 1.0%, the Reynolds number was between 1505.77 and 4517.32; for a volume of 1.5%, the Reynolds number was between 1441.05 and 4323.14; and for a volume of 2.0%, the Reynolds number was between 1393.75 and 4181.24.

# 4.1 Entropy Generation Ratio (EGR)

Entropy production quantifies the degree of irreversibility shown by the miniature heat sink. As the value of entropy generation increases, the performance of the system deteriorates. Hence, the examination of entropy creation was considered a crucial factor in designing efficient cooling systems. The entropy generation ratio was estimated using the following values [38, 39].

$$\Psi_{gen,total} = \Psi_{gen,th} + \Psi_{gen,f} \tag{12}$$

$$\Psi_{gen,th} = \left(\frac{q^2 D}{4T_{ava}^2 m_{na} c_f S t_f}\right) \tag{13}$$

$$\Psi_{gen,total} = \Psi_{gen,th} + \Psi_{gen,f}$$

$$\Psi_{gen,th} = \begin{pmatrix} q^{2}D \\ 4T_{avg}^{2}m_{ng}c_{f}St_{f} \end{pmatrix}$$

$$\Psi_{gen,f} = \begin{pmatrix} 2m^{3}\xi \\ \rho_{f}^{2}T_{avg}DA \end{pmatrix}$$

$$(12)$$

$$(13)$$

$$q = \left(\frac{Q_{avg}}{A}\right) \tag{15}$$

but 
$$Q_h = V.I$$
, and  $Q_a = \dot{m}.C_n.(T_0 - T_i)$  (16)

$$St_f = \left(\frac{Nu_f}{Re_f Pr_f}\right) = \left(\frac{h_f}{\rho_f C_{p,f} v_f}\right) \tag{17}$$

$$Nu = \frac{hD}{k}; Re = \frac{\rho vD}{\mu}; Pr = \frac{\mu c_p}{k}$$
 (18)

$$q = \left(\frac{Q_{avg}}{A}\right) \qquad (15)$$

$$Q_{avg} = \frac{(Q_h + Q_a)}{2},$$
but  $Q_h = V.I$ , and  $Q_a = \dot{m}.C_p.(T_0 - T_i) \qquad (16)$ 

$$St_f = \left(\frac{Nu_f}{Re_f Pr_f}\right) = \left(\frac{h_f}{\rho_f C_{p,f} v_f}\right) \qquad (17)$$

$$Nu = \frac{hD}{k}; \quad Re = \frac{\rho vD}{\mu}; \quad Pr = \frac{\mu C_p}{k} \qquad (18)$$

$$Whereas, h_f = \frac{Q_{avg}}{A(T_{wall} - T_{bulk})} \qquad (19)$$

$$But, A = \pi DL; \quad T_{wall} = \frac{T_1 + T_2 + T_3 + T_4}{4};$$

$$T_{bulk} = \frac{T_o + T_i}{2}; \ T_{avg} = \left[\frac{(T_i - T_o)}{ln(\frac{T_i}{T_o})}\right]$$
 (20)  
Friction factor,  $\xi = \frac{\Delta P}{\left(\frac{L}{d_i}\right)\left(\frac{\rho v^2}{2}\right)}$ 

Friction factor, 
$$\xi = \frac{\Delta P}{\left(\frac{L}{d_i}\right)\left(\frac{\rho v^2}{2}\right)}$$
 (21)

Entropy generation ratio,

$$(EGR) = \frac{(\Psi_{gen,total})_{nf}}{(\Psi_{gen,total})_{bf}}$$
(22)

From Eq. (13), the hybrid nanofluids thermal entropy generation  $(\Psi_{gen,th})$  was estimated and its data was presented in Fig. 4(a). The  $\Psi_{gen,th}$  was lower when  $\phi$  and Re was higher. The lower values of 13.57%, 19.21%, 23.94%, and 27.30% were observed at 0.5%, 1.0%, 1.5%, and 2.0% volume of nanofluids, respectively, at Reynolds numbers of 1726.1, 1505.77, 1441.05, and 1393.75, compared to the base fluid. Apparently, the further  $\Psi_{gen,th}$  was lowered by 17.92%, 22.84%, 28.73%, and 34.87% at 0.5%, 1.0%, 1.5%, and 2.0% vol. of hybrid nanofluids at Re of 5178.4, 4517.32, 4323.14, and 4181.24, when validated with the base fluid.

The use of highly conductive nanoparticles enhances heat conductivity and improves the Nusselt number in the base fluid. Furthermore, the movement of nanoparticles enhances the spread of heat in the flow field, resulting in a higher overall temperature of the flow, which is consequently reflected in the  $\Psi_{gen,th}$  drops. In addition, the inclusion of particles, the  $\Psi_{gen,f}$  results were increased in shear stress between particles, leading to an elevation in frictional pressure drop.

The recent investigation on rGO/ND hybrid nanofluids clearly demonstrates that the  $\Psi_{qen,th}$ declines with increasing Reynolds number and nanoparticle concentration. The reason for this was that the hybrid nanofluids have a greater conductivity compared to the base fluid due to the presence of suspended nanoparticles. thermophysical properties of the nanoparticles and the random motion of the particles also contribute to the increase in the Nusselt number for the rGO/ND nanofluid. Thermophysical characteristics were experimentally measured in the present study. demonstrated Ιt that enhancing thermophysical properties led to a higher heat transfer coefficient as the volume of particles rose.

From Eq. (14), the hybrid nanofluids frictional entropy generation  $(\Psi_{gen,f})$  was estimated and its data was presented in Fig. 4(b). The  $\Psi_{qen,f}$  was increased by 3.66%, 9.44%, 13.49%, and 17.23% at 0.5%, 1.0%, 1.5%, and 2.0% vol. of nanofluids at Re of 1726.1, 1505.77, 1441.05, and 1393.75, against base fluid. The  $\Psi_{qen,f}$  was higher by 6.48%, 12 .04%,

17.59%, and 21.30% at 0.5%, 1.0%, 1.5%, and 2.0% of hybrid nanofluids at Re of 5178.4, 4517.32, 4323.14, and 4181.24, when validated with base

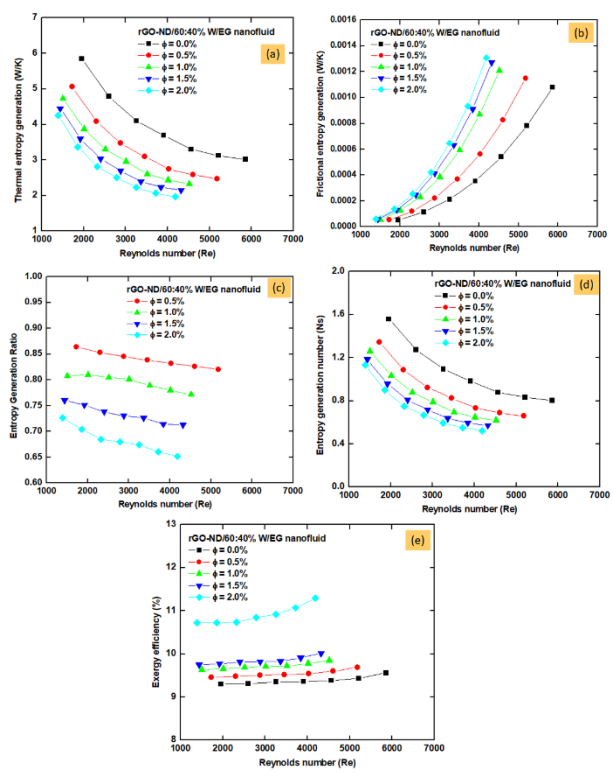


Fig. 4. Experimental data of rGO/ND nanofluids: (a) Thermal entropy generation, (b) frictional entropy generation, (c) entropy generation ratio, (d) entropy generation number, and (e) exergy efficiency

From Eq. (12), total entropy generation was estimated for both base fluid and nanofluids. From Eq. (22), the entropy generation ration (EGR) was calculated and the data was shown in Fig. 4(c). The EGR was ratio between nanofluids total entropy and base fluid total entropy. The EGR was decreased with the increase of  $\phi$  value, and Re value. The decrease of EGR stands for the deduction of irreversibilities. For the case of nanofluids, the EGR was very low against base fluid; which means the utilization of hybrid nanofluids eliminates the irreversibilities and increases the second law efficiency of the heat sink system.

#### 4.2 Entropy Generation Number

The entropy generation number (Ns) was evaluated from (Manay et a. [40]):

$$Ns = \frac{\Psi_{gen,total} \times T_{avg}}{q} \tag{23}$$

Entropy generation number (Ns) obtained from Eq. (23) was given in Fig. 4(d). The Ns was lowered by 13.62%, 19.26%, 24.10%, and 27.32% at 0.5%,

1.0%, 1.5%, and 2.0% vol. of nanofluids at Re of 1726.1, 1505.77, 1441.05, and 1393.75, against base fluid. The Ns was lowered by 18.12%, 23.25%, 29.02%, and 35.12% at 0.5%, 1.0%, 1.5%, and 2.0% of hybrid nanofluids at Re of 5178.4, 4517.32, 4323.14, and 4181.24, when validated with base fluid.

### 4.3 Exergy Efficiency

Exergy efficiency was estimated from Eq. (24),

$$\eta_{ex} = 1 - \frac{\Psi_{gen,th} \times T_{avg}}{\left[1 - \left(\frac{T_a}{T_c}\right)\right]q} \tag{24}$$

The data shown in Fig. 4(e) from the Eq. (24) for  $\eta_{ex}$  of nanofluids were increased by 1.72%, 3.55%, 4.84%, and 15.27% at 0.5%, 1.0%, 1.5%, and 2.0% vol. of nanofluids at Re of 1726.1, 1505.77, 1441.05, and 1393.75, against the base fluid. The  $\eta_{ex}$  was larger by 1.36%, 3.03%, 4.71%, and 18.10% at 0.5%, 1.0%, 1.5%, and 2.0% of hybrid nanofluids at Re of 5178.4, 4517.32, 4323.14, and 4181.24, over base fluid.

#### 4.4 PSO Results

The proposed approach initially has one hidden layer with a random size of neurons. The initial population size was 35 for PSO. PSO optimizes the number of layers and layer size by updating its particle position and velocity and evaluating the MSE of the ANN with different configurations. Fig. 5 illustrates the evaluation of the fitness function over the course of the iterations. The optimized ANN has two hidden layers, each with 10 neurons. The bias and weights of neurons are calculated using the training dataset. Later, the overall dataset was divided into 85% of the training and 15% of the test dataset. The optimized ANN was trained using a training dataset and the trained network was validated using a test dataset. The performance of the network was evaluated using MSE, RMSE, and R<sup>2</sup> scores.

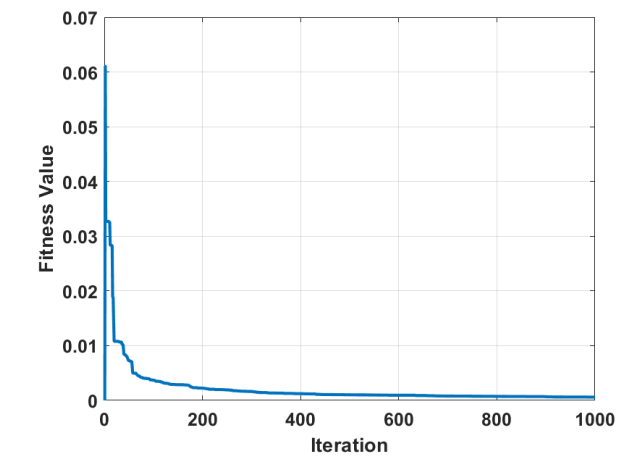


**Fig. 5.** The evaluation of the fitness function over the iteration

# 4.4.1 Thermal Entropy Generation

A total of 35 data points of thermal entropy were used for the PSO model, in which 29 and 6 were considered for train and testing the values. From model,  $R^2$ , MSE, and RMSE were analyzed, and their outcomes are indicated in Figs. 6(a-i). The experimental  $\Psi_{(gen,th)}$  data and the PSO  $\Psi_{(gen,th)}$  were almost matching with each other. For the case of train data, the MSE was 2.35e-03, and RMSE was 4.84e-02. Similarly, for the test data, the MSE was 8.44e-03, and RMSE was 9.19e-02. Additionally, for the all data, the MSE was 3.40e-03, and RMSE was 5.83e-02. The  $R^2$  values for train data was 0.99882, for test data was 0.99848, and for all data was 0.99811, respectively.

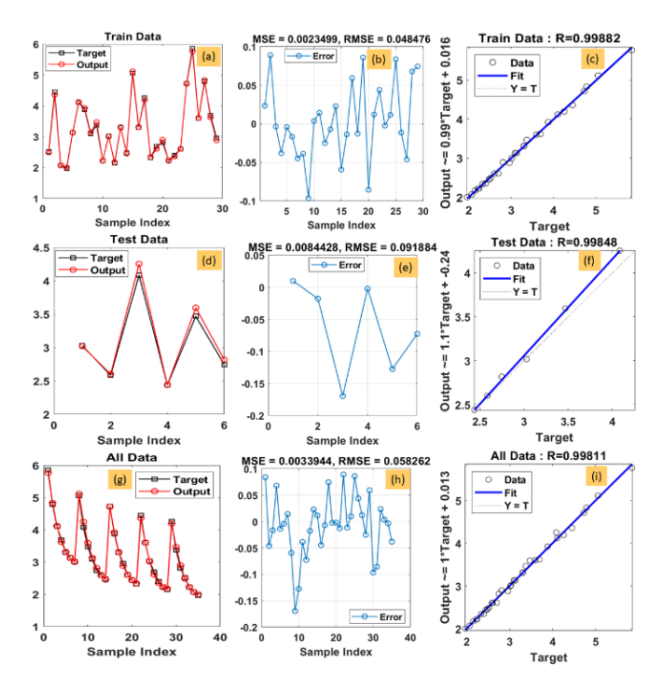


**Fig. 6**. PSO predictions of thermal entropy generation of rGO/ND nanofluids

#### 4.4.2. Frictional Entropy Generation

A total of 35 data points of  $\Psi_{(gen,f)}$  were used for the PSO model, in which 29 and 6 were considered for train and testing the values. From model, R², MSE, and RMSE were analyzed, and their outcomes are indicated in Figs. 7(a-i). The experimental  $\Psi_{(gen,f)}$  and the PSO  $\Psi_{(gen,f)}$  was almost matching with each other. For the case of train data, the MSE was 2.40e-9, and RMSE was 4.90e-05. Similarly, for the test data, the MSE was 2.46e-09, and RMSE was 4.96e-05. Additionally, for the all data, the MSE was 2.41e-09, and RMSE was 4.91e-05. The  $R^2$  values for train data was 0.99279, for test data was 0.99805, and for all data was 0.99218, respectively.

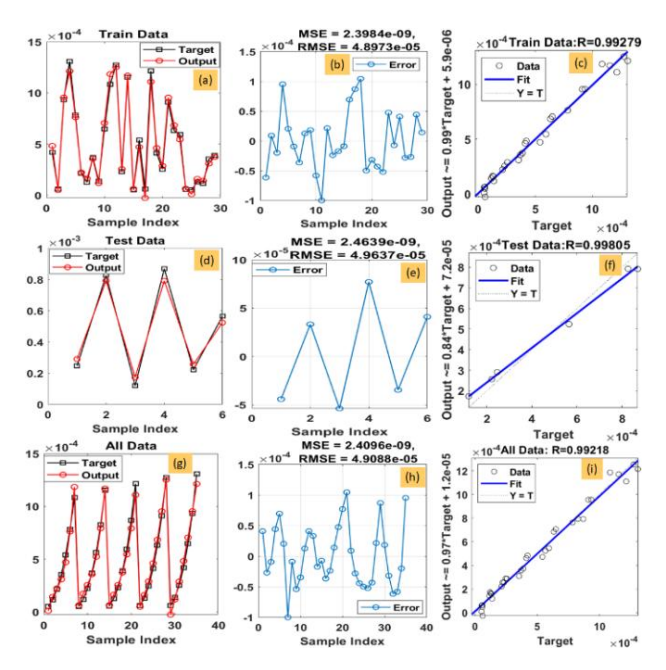


**Fig. 7.** PSO predictions of frictional entropy generation of rGO/ND nanofluids

# 4.4.3. Entropy Generation Ratio

A total of 30 data points of EGR were used for the PSO model, in which 25 and 5 were used for train and testing the values. From model,  $R^2$ , MSE, and RMSE were analyzed, and their values are provided in Figs. 8(a-i). The experimental EGR, and the PSO EGR data was almost matching with each other. For the case of train data, the MSE was 6.44e-06, and RMSE was 2.54e-03. Similarly, for the test data, the MSE was 3.83e-05, and RMSE was 6.18e-03. Additionally, for the all data, the MSE was 1.21e-05, and RMSE was 3.48e-03. The  $R^2$  values for train data was 0.9926, for test data was 0.98956, and for all data was 0.99849, respectively.

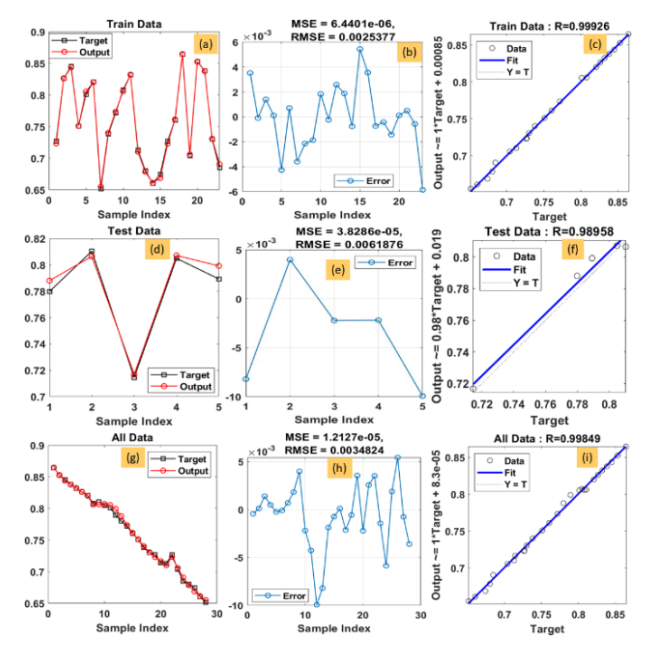


**Fig. 8.** PSO predictions of entropy generation ratio of rGO/ND nanofluids

# 4.4.4. Entropy Generation Number

A total of 35 data points of Ns were used for the PSO model, in which 29 and 6 were utilized for train and testing the values. From model, the  $R^2$ , MSE, and RMSE were analyzed, and its data is indicated in Figs. 9(a-i). The experimental Ns and the PSO Ns was almost matched with each other. For the case of train data, the MSE was 1.66e-04, and RMSE was 1.29e-02. Similarly, for the test data, the MSE was 0.000599, and RMSE was 0.024475. Additionally, for the all data, the MSE was 2.41e-04, and RMSE was 1.55e-02. The  $R^2$  values for train data was 0.99882, for test data was 0.99848, and for all data was 0.99811, respectively.

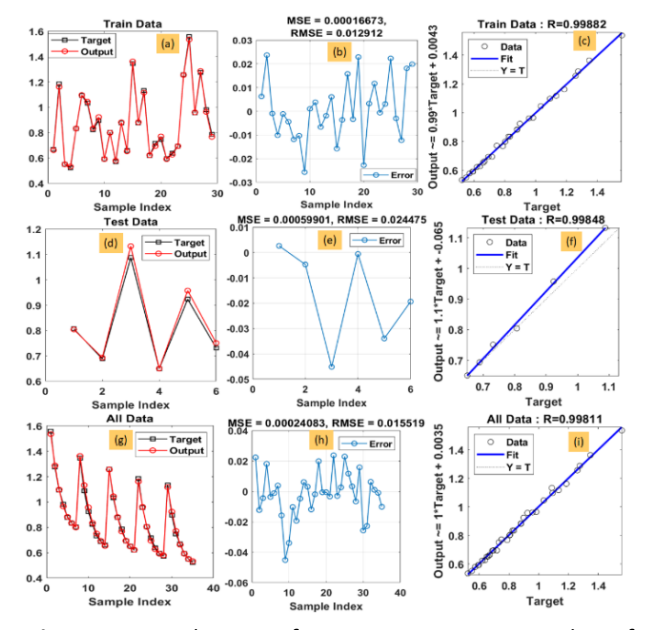


**Fig. 9.** PSO predictions of entropy generation number of rGO/ND nanofluids

#### 4.4.5. Exergy Efficiency

A total of 35 data points of  $\eta_{\rm ex}$  were used for the PSO model, in which 29 and 6 were utilized for train and testing the values. From model, the  $R^2$ , MSE, and RMSE were analyzed, and its data is indicated in Figs. 10(a-i). The experimental  $\eta_{\rm ex}$  and the PSO  $\eta_{\rm ex}$  were almost matched with each other. For the case of train data, the MSE was 0.001904, and RMSE was 0.043635. Similarly, for the test data, the MSE was 0.0059657, and RMSE was 0.077238. Additionally, for the all data, the MSE was 0.0026003, and RMSE was 0.050993. The  $R^2$  values for train data was 0.9972, for test data was 0.96283, and for all data was 0.99571, respectively.

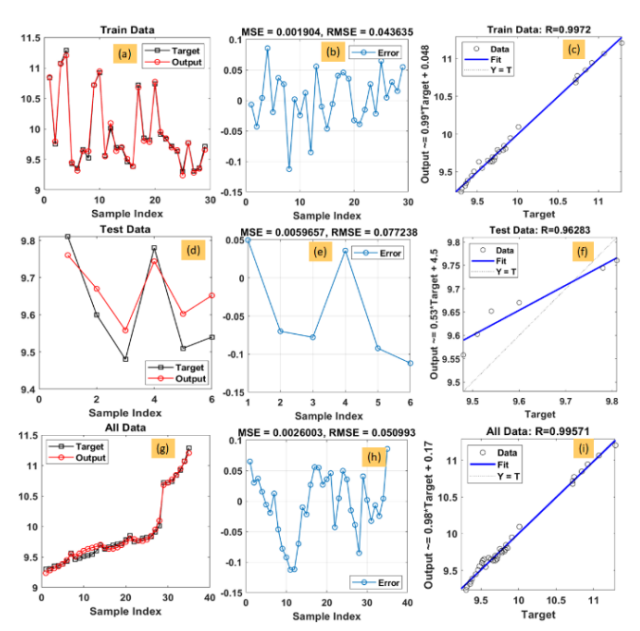


**Fig. 10.** PSO predictions of exergy efficiency of rGO/ND nanofluids

# 4.5. Proposed Correlations

Through the experimental data, the new correlations were developed.

$$\Psi_{qen.th} = 6.51183 - 0.000714Re - 0.9815\phi \tag{25}$$

$$\Psi_{qen.f} = -0.00083 + 3.39e^{-7}Re + 0.00023\phi$$
 (26)

$$Ns = 1.73 - 0.00019Re - 0.261450.03\phi \tag{27}$$

$$\eta_{ex} = 8.80971 + 0.00010Re + 0.724\phi \tag{28}$$

# 5. CONCLUSIONS

In order to cool the heat generated devices like processors in the computers mini-heat sink concept was used. However, the idea behind this research work was to consider the case where mini-heat was working with hybrid nanofluids, and to determine how much irreversibility may be decreased and how much exergy efficiency may be enhanced. To

understand this, an experimental study was conducted on a mini-heat sink operating with hybrid nanofluids under various volume loadings and mass flow rates. The stable 60:40% W/EG-based rGO/ND nanofluids were prepared and used in the experiments. Prior to the thermal entropy, and entropy tests, frictional hybrid nanofluids thermophysical properties were also estimated. The thermal conductivity of 2.0% vol. of rGO/ND nanofluids at 60°C was enhanced by 25.36%. Similarly, the viscosity of 2.0% vol. of nanofluid at 20°C was enhanced by a maximum of 96.60%, over the base fluid. At the same time, under 2.0% vol. the density was enhanced and specific heat was decreased. The thermal entropy generation of 2.0% vol. of hybrid nanofluid was decreased by 34.87%. Frictional entropy generation was raised by 21.3%, and exergy efficiency was raised by 18.10% at a Reynolds number of 4181.24 over the base fluid data.

To assess the accuracy and deviation of the experimentally measured data, a particle swarm optimization (PSO) machine learning algorithm was used. The entire dataset was spitted into train and test data. The obtained train and test data through the PSO was perfectly matched with the experimental data. From the PSO, the root-mean square errors of 0.058262, 4.9088e-5, 0.0034824, 0.015519, and 0.050993, with correlation coefficients of 0.99811, 0.99218, 0.99849, 0.99811, and 0.99571, were achieved for thermal entropy, frictional entropy, entropy generation ratio, entropy generation number, and exergy efficiency, respectively. As also noted through the R2, the deviation of the data was less than 10%. This means the experimental data were accurate and can be considered valid. Even with the use of nanofluids, the performance of the mini-heat was improved.

#### **CONFLICTS OF INTEREST**

The author declares no conflict of interest.

# **REFERENCES**

[1] V. Egan, J. Stafford, P. Walsh, E. Walsh, R. Grimes, An experimental study on the performance of miniature heat sinks for forced convection air cooling, 11<sup>th</sup> Intersociety Conference on Thermal and Thermomechanical Phenomena in Electronic Systems, Orlando, USA, 17 June 2008, 497–509.
https://doi.org/10.1109/ITHERM.2008.454431

https://doi.org/10.1109/ITHERM.2008.454431 0

- [2] M.M. Mohamed, M.A. El-Baky, Air cooling of mini-channel heat sink in electronic devices. *Journal of Electronics Cooling and Thermal Control*, 3, 2013: 49–57.
  - https://doi.org/10.4236/jectc.2013.32007
- [3] X.F. Peng, G.P. Peterson, Convective heat transfer and flow friction for water flow in microchannel structures. *International Journal of Heat and Mass Transfer*, 39(12), 1996: 2599–2608.
  - https://doi.org/10.1016/0017-9310(95)00327-
- [4] W. Qu, I. Mudawar, Experimental and numerical study of pressure drop and heat transfer in a single-phase micro-channel heat sink. *International Journal of Heat and Mass Transfer*, 45(12), 2002: 2459–2565. <a href="https://doi.org/10.1016/S0017-9310(01)00337-4">https://doi.org/10.1016/S0017-9310(01)00337-4</a>
- [5] J.S. Makam, N.B. Totla, Heat transfer characteristics of water cooled minichannel heat sink using different fluid flow geometries. *IOP Conference Series: Materials Science and Engineering*, 998, 2020: 012018. <a href="https://doi.org/10.1088/1757-899X/998/1/012018">https://doi.org/10.1088/1757-899X/998/1/012018</a>
- [6] S.E. Ghasemi, A.A. Ranjbar, S.M.J. Hoseini, Cooling performance analysis of water-cooled heat sinks with circular and rectangular minichannels using finite volume method. *Iranian Journal of Chemistry and Chemical Engineering*, 37(2), 2018; 231–239. https://doi.org/10.30492/ijcce.2018.26848
- [7] S.U.S. Choi, J.A. Eastman, Enhancing thermal conductivity of fluids with nanoparticles. ASME International Mechanical Engineering Congress & Exposition, 12-17 November 1995, San Francisco, USA, pp. 99–103.
- [8] S. Mukherjee, S. Wciślik, V. Khadanga, P.C. Mishra, Influence of nanofluids on the thermal performance and entropy generation of varied geometry microchannel heat sink. *Case Studies in Thermal Engineering*, 49, 2023: 103241. https://doi.org/10.1016/j.csite.2023.103241
- [9] S.J. Thrush, A.S. Comfort, J.S. Dusenbury, Y. Xiong, H. Qu, X. Han, J.D. Schall, G.C. Barber, X. Wang, Stability, thermal conductivity, viscosity, and tribological characterization of zirconia nanofluids as a function of nanoparticle concentration. *Tribology Transactions*, 63(1), 2019: 68–76.
  - https://doi.org/10.1080/10402004.2019.1660 017

- [10] B. Barbés, R. Páramo, E. Blanco, C. Casanova, Thermal conductivity and specific heat capacity measurements of CuO nanofluids. *Journal of Thermal Analysis and Calorimetry*, 115, 2014: 1883–1891. https://doi.org/10.1007/s10973-013-3518-0
- [11] R. Agarwal, K. Verma, N.K. Agrawal, R. Singh, Sensitivity of thermal conductivity for Al<sub>2</sub>O<sub>3</sub> nanofluids. *Experimental Thermal and Fluid Science*, 80, 2017: 19–26. <a href="https://doi.org/10.1016/j.expthermflusci.2016">https://doi.org/10.1016/j.expthermflusci.2016</a> .08.007
- [12] R. Chein, G. Huang, Analysis of microchannel heat sink performance using nanofluids. Applied Thermal Engineering, 25, 2005: 3104– 3114. <a href="https://doi.org/10.1016/j.applthermaleng.200">https://doi.org/10.1016/j.applthermaleng.200</a> 5.03.008
- [13] J. Lee, I. Mudawar, Assessment of the effectiveness of nanofluids for single-phase and two-phase heat transfer in micro-channels. *International Journal of Heat and Mass Transfer*, 50(3-4), 2007: 452–463. <a href="https://doi.org/10.1016/j.ijheatmasstransfer.2">https://doi.org/10.1016/j.ijheatmasstransfer.2</a> 006.08.001
- [14] M.A. Sheik, N. Beemkumar, A. Gupta, A. A. Gill, Y. Devarajan, R. Jayabal, G.M. Lionus Leo, Study the effect of silicon nanofluid on the heat transfer enhancement of triangular-shaped open microchannel heat sinks. *Silicon*, 16, 2024: 277–293.
  - https://doi.org/10.1007/s12633-023-02663-5
- [15] H.R. Seyf, S. Keshavarz Mohammadian, Thermal and hydraulic performance of counterflow microchannel heat exchangers with and without nanofluids. *ASME Journal of Heat and Mass Transfer*, 133(8), 2011: 081801. https://doi.org/10.1115/1.4003553
- [16] N.A.C. Sidik, Convective heat transfer and flow enhancement using nanofluids in divergentconvergent minichannel heatsink. AIP Conference Proceedings, 2689, 2023: 030012. https://doi.org/10.1063/5.0117544
- [17] P. Selvakumar, S. Suresh, Convective performance of CuO/water nanofluid in an electronic heat sink. *Experimental Thermal and Fluid Science*, 40, 2012: 57–63. <a href="https://doi.org/10.1016/j.expthermflusci.2012">https://doi.org/10.1016/j.expthermflusci.2012</a> .01.033
- [18] S.A. Fazeli, S.M.H. Hashemi, H. Zirakzadeh, M. Ashjaee, Experimental and numerical investigation of heat transfer, in a miniature heat sink utilizing silica nanofluid. *Superlattices Microstructure*, 51(2), 2012: 247–264.

# https://doi.org/10.1016/j.spmi.2011.11.017

- [19] C.T. Nguyen, G. Roy, C. Gauthier, N. Galanis, Heat transfer enhancement using Al<sub>2</sub>O<sub>3</sub>-water nanofluids for an electronic liquid cooling system. Applied Thermal Engineering, 27(8-9), 2007: 1501-1506.
  - https://doi.org/10.1016/j.applthermaleng.200 6.09.028
- [20] C.J. Ho, S.-T. Hsu, T.-F. Yang, B.-L. Chen, S. Rashidi, W.-M. Yan, Cooling performance of mini-channel heat sink with water-based nano-PCM emulsion-An experimental International Journal of Thermal Sciences, 164, 2021: 106903.
  - https://doi.org/10.1016/j.ijthermalsci.2021.10 6903
- [21] C.J. Ho, W.C. Chen, An experimental study on thermal performance of Al<sub>2</sub>O<sub>3</sub>/water nanofluid in a minichannel heat sink. Applied Thermal Engineering, 50(1), 2013: 516-522. https://doi.org/10.1016/j.applthermaleng.201

2.07.037

- [22] A.K. Patel, S.P.S. Rajput, R. Kumar, A. Sharma, A.P. Singh, M.K. Sharma, P. Goyal, P. Singhal, Design and heat transfer performance analysis of mini-channel heat sink with water, EG and **EG20** nanofluids-computational based approach. International Journal on Interactive Design and Manufacturing, 18(33), 2024: 2119-2130.
  - https://doi.org/10.1007/s12008-022-00951-9
- [23] Z.H. Saadoon, F.H. Ali, H.K. Hamzah, A.M. Abed, M. Hatami, Improving the performance of mini-channel heat sink by using wavy channel and different types of nanofluids, Scientific Reports, 12, 2022: 9402.
  - https://doi.org/10.1038/s41598-022-13519-0
- [24] L.S. Sundar, M.K. Singh, A.C.M. Sousa, Enhanced heat transfer and friction factor of MWCNT–Fe<sub>3</sub>O<sub>4</sub>/water hybrid nanofluids. International Communications in Heat and Mass Transfer, 52, 2014: 73-83.
  - https://doi.org/10.1016/j.icheatmasstransfer. 2014.01.012
- [25] L.S. Sundar, G.O. Irurueta, E.V. Ramana, M.K. Singh, A.C.M. Sousa, Thermal conductivity and viscosity of hybrid nanofluids prepared with magnetic nanodiamond-cobalt oxide (ND-Co<sub>3</sub>O<sub>4</sub>) nanocomposite, Case Studies in Thermal Engineering, 7, 2016: 66-77.
  - https://doi.org/10.1016/j.csite.2016.03.001
- [26] L.S. Sundar, E.V. Ramana, M.P.F. Graça, M.K. Singh, A.C.M. Sousa, Nanodiamond-Fe<sub>3</sub>O<sub>4</sub> nanofluids: Preparation and measurement of

- viscosity, electrical and thermal conductivities. International Communications in Heat and Mass Transfer, 73, 2016: 62-74. https://doi.org/10.1016/j.icheatmasstransfer. 2016.02.013
- [27] I. Wole-Osho, E.C. Okonkwo, H. Adun, D. Kavaz, S.Abbasoglu, An intelligent approach to predicting the effect of nanoparticle mixture ratio, concentration and temperature on thermal conductivity of hybrid nanofluids. Journal of Thermal Analysis and Calorimetry, 144, 2021: 671-688.
  - https://doi.org/10.1007/s10973-020-09594-y
- [28] A.S. Dalkılıc, G. Yalçın, B.O. Küçükyıldırım, S. Öztuna, A.A. Eker, C. Jumpholkul, S. Nakkaew, S. Wongwises, Experimental study on the thermal conductivity of water-based CNT-SiO<sub>2</sub> hvbrid nanofluids. International Communications in Heat and Mass Transfer, 99, 2018: 18-25.
  - https://doi.org/10.1016/j.icheatmasstransfer. 2018.10.002
- [29] Ç. Yıldız, M. Arıcı, H. Karabay, Comparison of a theoretical and experimental thermal conductivity model on the heat transfer performance of Al<sub>2</sub>O<sub>3</sub>-SiO<sub>2</sub>/water hybridnanofluid. International Journal of Heat and Mass Transfer, 140, 2019: 598-605. https://doi.org/10.1016/j.ijheatmasstransfer.2
  - 019.06.028
- [30] G.M. Moldoveanu, G. Huminic, A.A. Minea, A. Huminic, Experimental study on thermal conductivity of stabilized Al<sub>2</sub>O<sub>3</sub> and SiO<sub>2</sub> nanofluids and their hybrid. International Journal of Heat and Mass Transfer, 127 (Part A), 2018: 450–457.
  - https://doi.org/10.1016/j.ijheatmasstransfer.2 018.07.024
- [31] G. Sriharan, S. Harikrishnan, H.F. Oztop, A thermophysical review properties, preparation, and heat transfer enhancement of conventional and hybrid nanofluids utilized in micro and mini channel heat sink. Sustainable Energy Technologies and Assessments, 58 2023: 103327.
  - https://doi.org/10.1016/j.seta.2023.103327
- [32] T. Baig, H.A. Tariq, M. Anwar, A.A. Shoukat, H.M. Ali, M.M. Janjua, Hydrothermal performance of mini-channel heat sink using nanofluids/hybrid nanofluids: A numerical study. Energy Sources, Part A: Recovery, Utilization, and Environmental Effects, 46(1), 2024: 4628-4646.

- https://doi.org/10.1080/15567036.2024.2323 155
- [33] G. Sriharan, S. Harikrishnan, H.M. Ali, Enhanced heat transfer characteristics of the mini hexagonal tube heat sink using hybrid nanofluids, *Nanotechnology*, 33, 2022: 475403 https://doi.org/10.1088/1361-6528/ac8995
- [34] V. Kumar, J. Sarkar, Numerical and experimental investigations on heat transfer and pressure drop characteristics of Al<sub>2</sub>O<sub>3</sub>-TiO<sub>2</sub> hybrid nanofluid in minichannel heat sink with different mixture ratio. *Powder Technology*, 345, 2019: 717–727.

https://doi.org/10.1016/j.powtec.2019.01.061

- [35] V. Kumar, J. Sarkar, Two-phase numerical simulation of hybrid nanofluid heat transfer in minichannel heat sink and experimental validation. *International Communications in Heat and Mass Transfer*, 91, 2018: 239–247. <a href="https://doi.org/10.1016/j.icheatmasstransfer.2017.12.019">https://doi.org/10.1016/j.icheatmasstransfer.2017.12.019</a>
- [36] N.I. Zaaba, K.L. Foo, U. Hashim, S.J.Tan, Wei-Wen Liu, C.H. Voon, Synthesis of Graphene Oxide using Modified Hummers Method:

- Solvent Influence. *Procedia Engineering*, 184, 2017: 469–477.
- https://doi.org/10.1016/j.proeng.2017.04.118
- [37] L.S. Sundar, Heat transfer, friction factor and exergy efficiency analysis of nanodiamond-Fe<sub>3</sub>O<sub>4</sub>/water hybrid nanofluids in a tube with twisted tape inserts. *Ain Shams Engineering Journal*, 14(9), 2023: 102068. https://doi.org/10.1016/j.asej.2022.102068
- [38] M. Rahimi-Gorji, O. Pourmehran, M. Hatami, D.D. Ganji, Statistical optimization of microchannel heat sink (MCHS) geometry cooled by different nanofluids using RSM analysis. *The European Physical Journal Plus*, 130, 2015: 22.
  - https://doi.org/10.1140/epjp/i2015-15022-8
- [39] M.M. Awad, A review of entropy generation in microchannels. *Advances in Mechanical Engineering*, 7(12), 2015: 1687814015590297. https://doi.org/10.1177/1687814015590297
- [40] E. Manay, E.F. Akyürek, B. Sahin, Entropy generation of nanofluid flow in a microchannel heat sink. *Results Physics*, 9, 2018: 615–624. https://doi.org/10.1016/j.rinp.2018.03.013